



The role of external far-ultraviolet irradiation in the survival of astrophysical ices in Elias 29

W. R. M. Rocha^{1,2}★ and S. Pilling^{1,3}

¹*Instituto de Pesquisa e Desenvolvimento (IP&D), Universidade do Vale do Paraíba, Av. Shishima Hifumi 2911, São José dos Campos SP, CEP 12244-000, Brazil*

²*SUPA, School of Physics & Astronomy, University of St Andrews, North Haugh, St Andrews KY16 9SS*

³*Departamento de Física, Instituto Tecnológico de Aeronáutica, ITA – DCTA, Vila das Acácias, São José dos Campos SP, CEP 12228-900, Brazil*

Accepted 2018 May 29. Received 2018 April 27; in original form 2018 January 31

ABSTRACT

The survival of astrophysical ices in star-forming regions depends on the suitability of temperature, density and radiation conditions. In this article, the role of the interstellar radiation field (ISRF) on ices in Elias 29 is addressed. This object is the most luminous protostar in the ρ Oph E molecular cloud and is surrounded by many young stellar objects only a few arcmin distant. In addition, two other bright BV stars (S1 and HD 147889) enhance the external irradiation in Elias 29. This study was carried out using the Monte Carlo radiative transfer code RADMC-3D assuming internal and external irradiation. As result, we found that HD 147889 dominates the ISRF, rather than the closest protostars, and contributes to enhancing the external irradiation by 44 times the standard value. Furthermore, remarkable effects are observed in the far-infrared (FIR) spectrum, as well as in the near-infrared (near-IR) image. Additionally, the snowline positions of volatile compounds, such as CO, O₂, N₂ and CH₄, are redefined to a toroidal-shaped morphology in the envelope, with low far-ultraviolet (FUV) flux (10^{-7} erg cm⁻² s⁻¹). In such a scenario, the formation of complex molecules as the result of hydrogenation or oxygenation of volatile species is expected to be severely affected.

Key words: astrochemistry – radiative transfer – stars: individual: Elias 29 – stars: pre-main-sequence.

1 INTRODUCTION

The gravitational collapse of molecular clouds is followed by hierarchical fragmentation that breaks up a large molecular cloud into smaller cores to form low-mass stars (Larson 1978; Klessen, Burkert & Bate 1998). In such a star-forming region scenario, it is expected that all young stellar objects (YSOs) are externally heated by neighbourhood protostars, once they increase the far-ultraviolet (FUV) interstellar radiation field (ISRF) by a few orders of magnitude. The standard ISRF might be defined as a function of the ultraviolet (UV) Draine field (Draine & Bertoldi 1996; Röllig et al. 2007: $\chi_{\text{ISRF}} = 1$) integrated between 91.2 and 205 nm (FUV regime) to ensure coverage of important photochemical processes such as photodissociation (van Dishoeck, Jonkheid & van Hemert 2006). The numerical integration for $\chi_{\text{ISRF}} = 1$ yields a flux of 1.921×10^8 cm⁻² s⁻¹.

Jørgensen et al. (2006) discuss some effects of strong external irradiation on protostellar envelopes in the Orion cloud. The authors report that the ISRF was increased to 10^3 – 10^4 times the standard

field and consequently the outer envelopes of protostars were heated above the desorption temperature of CO, i.e. larger than 25 K. Other regions, such as Corona Australis (CrA), were considered in Lindberg & Jørgensen (2012). Using mainly H₂CO rotational diagrams, they found that outer envelopes in CrA are heated up to 60 K by a closer Herbig Be star. This same region was probed later on by Lindberg et al. (2014), employing Atacama Large Millimeter/submillimeter Array (ALMA) observations. In conclusion, they state that evaporation of CO ice due to high temperature prevents the formation of complex organic molecules (COMs) in the CrA cloud.

Photodissociation regions (PDRs) can also be predicted by measuring the strength of the ISRF using fine-structure emission lines such as O I (63 and 145 μ m) and C II (158 μ m) at far-infrared (FIR) wavelengths. Je et al. (2015) observed the Class I protostar GSS30-IRS1 located in the Ophiuchus (Oph) cloud using the Photodetector Array Camera and Spectrometer (PACS) on board the *Herschel Space Observatory*. They report extended C II emission, which probes a PDR. The total C II intensity reveals that standard ISRF is enhanced by up to 20 in units of the Habing field (G_0). Indeed, the C II strong extended emission in ρ Oph was previously described in Liseau et al. (1999) as the result of external irradiation

* E-mail: willrobson88@hotmail.com

of around 10–120 G_0 originating in B2V star HD 147889. The origin of this emission might not be related to protostars themselves, but rather can probe PDRs in the outer parts of molecular clouds that host very embedded objects. The outer envelope, however, would be addressed by using H₂CO and c-C₃H₂ emission lines, as suggested by Lindberg et al. (2017). The authors also estimated that the temperature of the outer envelope in the Oph cloud (excluding the upper limits) varies between 20 and 50 K, due to the influence of two B-type stars: S1 and HD 147889.

Among the YSOs formed in the Ophiuchus cloud, Elias 29 is a Class I object, placed at ρ Oph E (α (J2000) = 16h27'09.42" and δ (J2000) = $-24^\circ 37'21.1''$), the distance and luminosity of which are respectively 120 pc and $16.5 L_\odot$ (Rocha & Pilling 2015, hereafter Paper I). As suggested in Paper I, the frozen molecules in Elias 29 have experienced chemical evolution driven by cosmic rays (CR), given the prominent absorption bands between 5 and 8 μm . However, many other objects formed in the vicinity of Elias 29 might play an important role in the survival of astrophysical ices in its envelope. In this article, photochemical processes such as photodesorption and photodissociation in Elias 29 and consequently the half-life of complex organic molecules formed by interstellar irradiation are discussed.

This article is structured as follows: Section 2 constrains the external irradiation in Elias 29 and introduces the physical parameters for the continuum radiative transfer simulation using the RADMC-3D code. In Section 3 we show the results and provide a discussion relative to the 0.1–10 000 μm Spectral Energy Distribution (SED), near-IR image, as well as the temperature profile in the outer envelope. Finally, Section 4 summarizes our conclusions.

2 METHODOLOGY

In this section, we show how the external UV radiation field in Elias 29 was constrained from the observational data and simulated by a radiative transfer model with the RADMC-3D¹ code.

2.1 External irradiation in the protostar Elias 29

A detailed study concerning external irradiation in the ρ Oph cloud was first provided by Liseau et al. (1999), although no specific statement about Elias 29 is presented. According to the authors, this cloud is surrounded by two potential sources of UV: HD 147889 (B2 V) and S1 (B3 V), although they conclude that HD 147889 dominates the radiation field in this scenario. S1 emission, on the other hand, only dominates in its neighbourhood, i.e. ρ Oph A, as described in Liseau et al. (2015) and Larsson & Liseau (2017).

The high illumination coming from HD 147889 produces PDR-type emission at the edges of the ρ Oph cloud (Liseau et al. 1999; Ceccarelli et al. 2002; Green et al. 2016), given the presence of the C II [158 μm] line detected by the Infrared Space Observatory (ISO), using the Long Wavelength Spectrometer (LWS) between 45 and 195 μm (Clegg et al. 1996), as shown in Fig. 1(a). This line, however, was detected in absorption by the PACS instrument on board the *Herschel Space Observatory*, with resolution power $R \sim 1000$ –3000, as reported by Green et al. (2013) and shown in Fig. 1(b). The reason is that *Herschel* effectively chops back and forth every 1/8 second between the target (Elias 29) and an off position a few arcmin away (~ 3 arcmin) and, since the [C II] was in

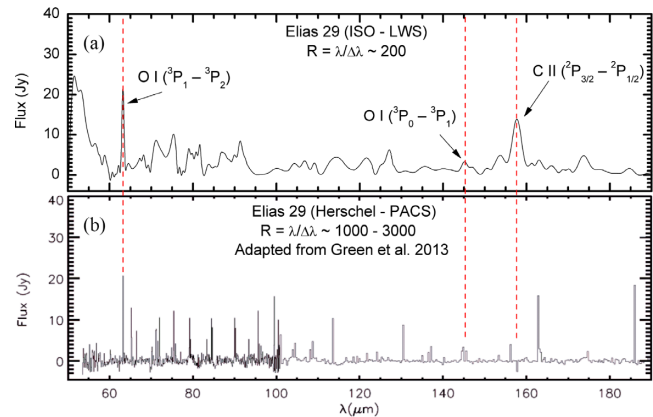


Figure 1. Continuum-subtracted spectrum of Elias 29 in the FIR. The fine-structure emission lines are indicated by arrows. Panel (a) shows an observation from *ISO* and (b) the spectrum obtained with the *Herschel Space Observatory* adapted from Green et al. (2013).

both positions, it is subtracted off (Green, private communication²). In addition, other lines usually associated with PDR emission, such as O I [63 and 145 μm] lines, were also detected using both *ISO* and *Herschel*. In particular, O I [63 μm] emission is centred on Elias 29, as shown in Green et al. (2013) and Riviere-Marichalar et al. (2016), and probably originates from the cavity walls illuminated by the central source given an almost face-on inclination (Boogert et al. 2002; Rocha & Pilling 2015). In this sense, these emission lines cannot be used to constrain the external irradiation of Elias 29 itself.

2.1.1 H₂CO emission as tracer of envelope temperature

A study of externally heated protostellar cores in the Oph cloud was recently carried out by Lindberg et al. (2017) using Atacama Pathfinder Experiment 218-GHz observations of molecular emission (H₂CO and c-C₃H₂) as tracers of envelope temperature. They state that H₂CO emission is able to trace the temperature for a radius $R > 2000$ au, whereas c-C₃H₂ originates in the inner regions of the envelope. In this way, the transition para-H₂CO [3₀₃–2₀₂] at 218.2222 GHz is reported, leading to an upper limit for rotational temperature of 109 K in Elias 29. The molecule c-C₃H₂, however, has not been observed. In this article, the rotational temperature was recalculated using three transitions reported by Boogert et al. (2002) obtained with the James Clerk Maxwell Telescope (JCMT) and the National Radio Astronomy Observatory (NRAO), as shown in Table 1.

Following Lindberg et al. (2017) and assuming that molecules are in local thermodynamic equilibrium (LTE), the upper-level column density (N_u) of formaldehyde was calculated using the following equations described in Goldsmith & Langer (1999):

$$N_u = \frac{8\pi k v^2}{hc^3 A_{ul} \eta_{mb}} \int T_{MB} dv, \quad (1)$$

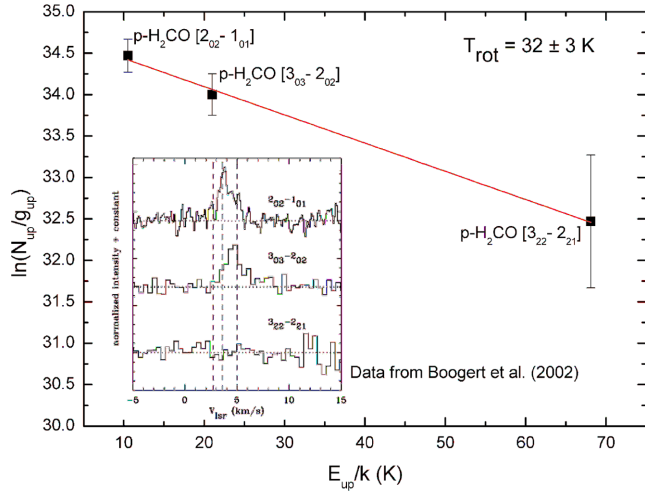
$$\ln \left(\frac{N_u}{g_u} \right) = \ln N_{\text{tot}} - \ln Q(T_{\text{rot}}) - \frac{E_u}{k T_{\text{rot}}}, \quad (2)$$

²Member of the ‘Dust, Ice and Gas In Time (DIGIT) Herschel Key Program’ team.

¹<http://www.ita.uni-heidelberg.de/~dullemond/software/radmc-3d/>

Table 1. Rotational parameters of para-H₂CO. Information extracted from Boogert et al. (2002) and Müller et al. (2001).

Molecule	Transition	ν (GHz)	E_u/k	A_{ul} (s^{-1})	g_u	η_{mb}	$\int T_{MB} dv$ [km s $^{-1}$]	Telescope
p-H ₂ CO	2 ₀₂ -1 ₀₁	145.6030	10.48	7.8×10^{-5}	5	0.81	0.39	NRAO
p-H ₂ CO	3 ₀₃ -2 ₀₂	218.2222	20.96	2.8×10^{-4}	7	0.68	0.82	JCMT
p-H ₂ CO	3 ₂₂ -2 ₂₁	218.4756	68.09	1.6×10^{-4}	7	0.68	<0.12	JCMT

**Figure 2.** Rotational diagram for three transitions of the para-H₂CO molecule.

where k , ν , h , c are the obvious physical constants. $\int T_{MB} dv$ is the integrated intensity, A_{ul} and η_{mb} are the spontaneous Einstein coefficient and beam efficiency, respectively. g_u is the degeneracy of the upper level, N_{tot} is the total column density of formaldehyde, $Q(T_{rot})$ is the partition function at the rotational temperature T_{rot} and E_u is the energy at the upper level.

The temperature in the outer envelope of Elias 29 calculated from the rotational diagram presented in Fig. 2 is $T_{rot} = 32 \pm 3$ K. This seems to be the mean temperature of the ρ Oph cloud, once the range calculated in Lindberg et al. (2017) is between 20 and 50 K, excluding the values shown as upper limits.

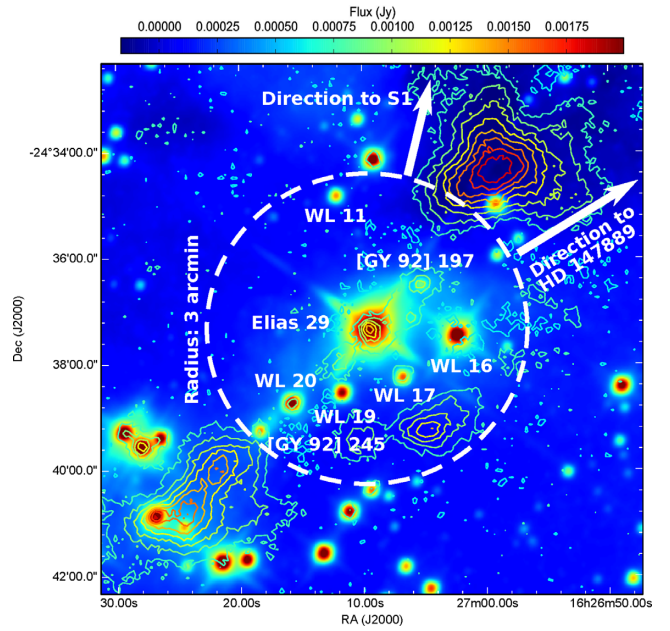
2.1.2 External irradiation constrained from flux extinction

Although B-type stars dominate UV irradiation in the ρ Oph cloud, the close YSOs around Elias 29 are also potential sources of heating. Fig. 3 shows a near-IR image (10×10 arcmin 2) obtained with the *Wide-field Infrared Survey Explorer* (WISE)³ at $3.4 \mu\text{m}$ centred on Elias 29. Contours indicate the cold dust emission at $850 \mu\text{m}$ obtained from SUBARU/James Clerk Maxwell Telescope (JCMT).⁴ This image shows that at least seven objects are distant from Elias 29 by a radius of 3 arcmin and these are listed in Table 2, as well as S1 and HD 147889.

Using the information provided in Table 2, Fig. 4(a) shows a 3D projection of each object inside the circle (Fig. 3) relative to Elias 29. The positions of S1 and HD 147889 relative to Elias 29 are shown in Fig. 4(b). Panels in Fig. 4 are illustrative, to show that it is convenient to assume an isotropic external irradiation in simulations, as will be shown in Section 2.2.

³irsa.ipac.caltech.edu/Mission/wise.html

⁴www.cadc-ccda.hia.nrc-cnrc.gc.ca/en/jcmt

**Figure 3.** WISE image centred on Elias 29 with a field of view (FOV) of 10×10 arcmin 2 . The colours represent the flux in Jy. The contours are the dust emission at $850 \mu\text{m}$ collected from SUBARU/JCMT in Jy pixel $^{-1}$. The dashed circle limits a region with radius of 3 arcmin. The arrows indicate the direction to S1 and HD 147889.

Once the environment around Elias 29 was characterized, the total incident flux was calculated, using the following equation:

$$F_{\text{tot}} = \sum_i^n \left(\frac{L_i^{\text{UV}}}{4\pi R_i^2} \right) \exp [\bar{\tau}_i^{\text{UV}}], \quad (3)$$

where F_{tot} is the total flux coming from neighbouring objects (i to n) around Elias 29 as shown in Table 2, L_i^{UV} is the UV luminosity and R_i the relative distance to the ρ Oph cloud. Fig. 5 was used to constrain the UV extinction between each object and Elias 29, assuming the relation $A_{\text{UV}} \approx 2A_V$ (Fitzpatrick 1999; Draine 2003). This figure shows a region of ρ Oph 10×10 arcmin 2 containing the visual extinction (A_V) map (Ridge et al. 2006). We employed the following equations to obtain the mean ultraviolet optical depth ($\bar{\tau}_i^{\text{UV}}$) along the distance R_i :

$$\bar{\tau}_i^{\text{UV}} = \left(\frac{2}{m} \sum_j^m A_V^{ij} - A_V^{\text{for}} \right) \rho_d^{\text{rel}} \frac{R_i}{d_i}, \quad (4)$$

where $\frac{2}{m} \sum_j^m A_V^{ij}$ is the mean UV extinction calculated from Fig. 5 along the pixels j to m between each object i and Elias 29, the visual extinction due to foreground clouds is estimated to be 11 mag (Boogert et al. 2002), ρ_d^{rel} is the local dust density relative to the interstellar medium (ISM), assumed to be 10^5 from Boogert

Table 2. List and characteristics of the objects presented in Fig. 3.

Object	RA (J2000) (h m s)	Dec. (J2000) (d m s)	Distance ^a (pc)	Relative distance ^j (pc)	L_{bol} (L_{\odot})	L_{UV}^l (L_{\odot})	$\overline{A_V^i}^m$ (mag)
WL 11	16 27 12.131	-24 34 49.14	128 ^b	6.5×10^{-3}	0.04 ^e	0.01	26.4
WL 16	16 27 02.340	-24 37 27.20	125 ^c	1.1×10^{-2}	250.00 ^c	10.30	26.4
WL 17	16 27 06.776	-24 38 15.20	137 ^d	1.4×10^{-2}	0.60 ^e	0.07	26.4
WL 19	16 27 11.776	-24 38 32.02	123 ^e	1.2×10^{-2}	58.00 ^e	3.05	28.4
WL 20	16 27 15.730	-24 38 43.70	110 ^f	8.3×10^{-3}	1.80 ^e	0.17	27.8
[GY92] 197	16 27 05.246	-24 36 29.79	100 ^g	1.4×10^{-2}	0.15 ^e	0.02	25.9
[GY92] 245	16 27 18.380	-24 39 14.68	105 ^h	6.0×10^{-3}	0.12 ^e	0.02	25.6
HD147889	16 25 24.317	-24 27 56.57	120 ⁱ	7.0×10^{-2}	4500.00 ^k	116.00	18.2
S1	16 26 34.167	-24 23 28.26	120 ⁱ	5.1×10^{-2}	1100.00 ^k	35.70	20.0

Notes: ^adistance from Earth; ^bKhanzadyan et al. (2004); ^cZhang et al. (2017); ^dOrtiz-León et al. (2017);

^eBontemps et al. (2001); ^fRessler & Barsony (2001); ^gJørgensen et al. (2008);

^hde Geus, de Zeeuw & Lub (1989); ⁱLindberg et al. (2017);

^jdistance between each object in the Oph cloud: <http://docs.astropy.org/en/stable/api/astropy.coordinates.SkyCoord.html>;

^kLiseau et al. (1999); ^l $\log_{10} L_{\text{UV}} = 0.836 \times \log_{10} L_{\text{bol}} - 1.78$ (Lee, Lee & Bergin 2015); ^msee text for details.

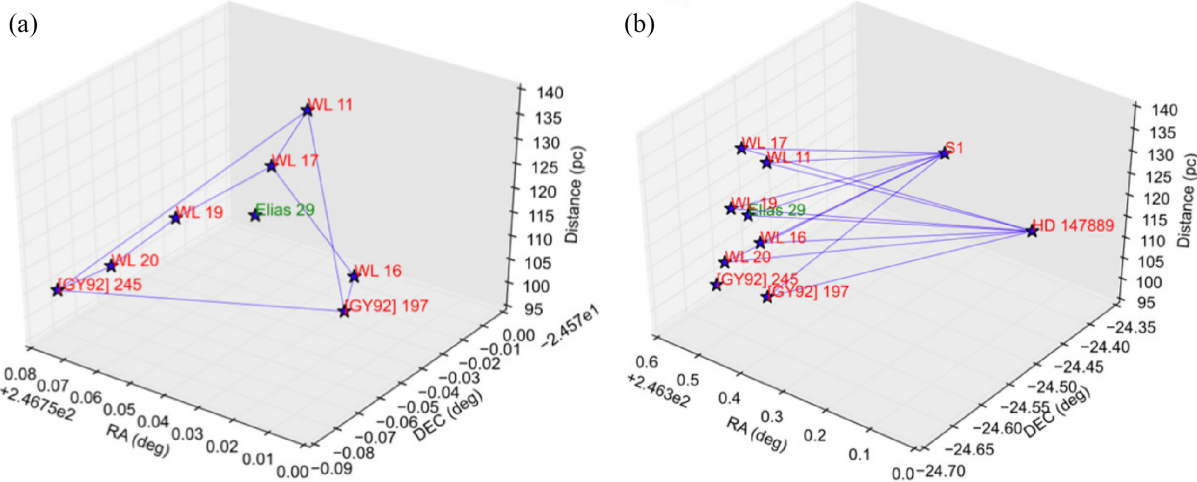


Figure 4. Three-dimensional spatial distribution of selected protostars in the ρ Oph cloud. (a) Star symbols are objects inside the dashed circle in Fig. 3 and Elias 29 is highlighted by a green label. The connections among the objects show that Elias 29 is embedded in a UV radiation field. (b) Same as panel (a), but now showing S1 and HD 147889 B-type stars that dominate the radiation field in the ρ Oph cloud. The connections are only to guide the eyes.

et al., and d_i is the distance of each object along the line of sight in parsecs (pc).

Using this methodology, it was found that the external irradiation interacting with Elias 29 is $44\chi_{\text{ISRF}}$. In percentage terms, HD 147889 contributes roughly 93 per cent of the external UV field, whereas S1, WL 16 and others contribute 5, 1.5 and 0.5 per cent, respectively.

2.2 Continuum radiative transfer simulation including internal and external irradiation

In order to understand how external irradiation affects the survival of ices in Elias 29, the RADMC-3D code was used. It performs a three-dimensional Monte Carlo radiative transfer calculation considering an axisymmetric density profile. Specifically, in this article, the code was used to calculate the dust temperature and total flux in Elias 29, but no gas distribution was assumed. Fig. 6 shows an illustration of the environment of Elias 29 and the region to which the RADMC-3D simulation is limited.

2.2.1 Disc and envelope parameters

The radiative transfer for internal irradiation was already simulated in Paper I and the physical parameters are shown in Table 3. The disc and envelope density profile were defined by using the following equations, as described in Paper I:

$$\rho_{\text{disc}}(r, \theta) = \frac{\Sigma_0 (r/R_0)^{-1}}{\sqrt{2\pi} H(r)} \exp \left[-\frac{1}{2} \left(\frac{r \cos \theta}{H(r)} \right)^2 \right], \quad (5)$$

$$\rho_{\text{env}} = \rho_0 \left(\frac{R_{\text{out}}}{r} \right), \quad (6)$$

where θ is the angle from the axis of symmetry; Σ_0 is the surface density at the outer radius R_0 and $H(r)$ is the disc scaleheight, given by $H(r) = r(H_0/R_0)(r/R_0)^{2/7}$, which is defined using the self-irradiated passive disc proposed by Chiang & Goldreich (1997). Further, ρ_0 is the density at the outer radius of the envelope R_{out} . Equation (5) was also used in models by Pontoppidan et al. (2005), Lommen et al. (2008) and Crapsi et al. (2008), whereas equation

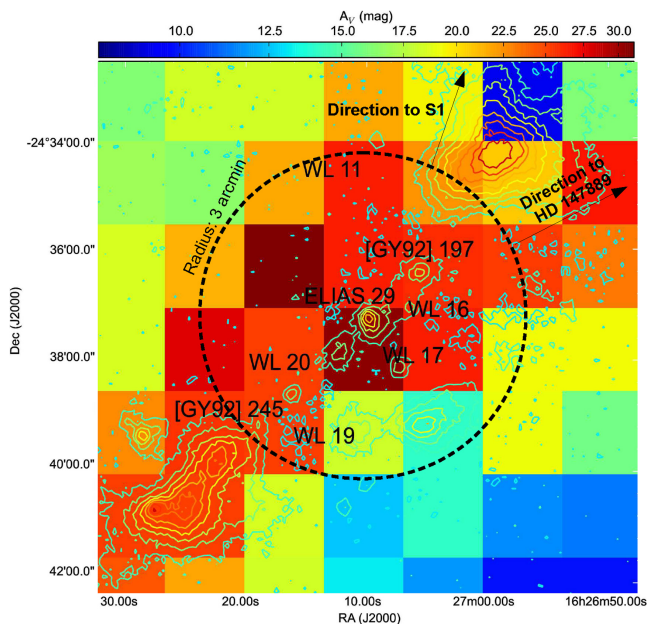


Figure 5. Visual extinction (A_V) map centered on Elias 29 with a FOV of 10×10 arcmin 2 , obtained from the Coordinated Molecular Probe Line Extinction Thermal Emission (COMPLETE) survey (Ridge et al. 2006). Contours, dashed circle and description are the same as in Fig. 3.

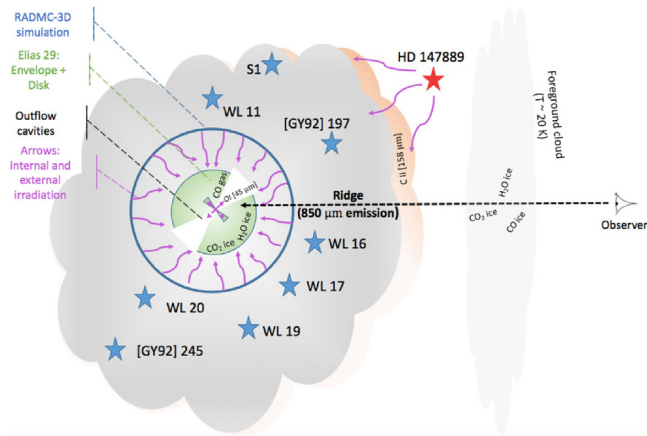


Figure 6. Schematic illustration of the Elias 29 environment. The disc inclination is 60° relative to the observer. The internal protostar and external objects are sources of photons in Elias 29, although HD 147889 dominates the external irradiation and might ionize the C atom. The figure is not to scale.

(6) was modified from Lommen et al. (2008) to characterize a static envelope, as used in Pontoppidan et al. (2005).

It is worth noting that different values for the disc dimension of Elias 29 are presented in the literature. Boogert et al. (2002) has fixed the disc size at 500 au, whereas Miotello et al. (2014) propose a size between 15 and 200 au by considering an optically thick or thin disc, respectively. As claimed by these authors, the first case is unrealistic because the dust properties cannot be addressed. In the second one, the disc should be populated by cm-sized pebbles. Huélamo et al. (2005) support the idea that the Elias 29 disc is around 200 au, due to a direct image in the K band obtained with the Very Large Telescope Infrared Spectrometer And Array Camera

Table 3. Physical parameters used in the radiative transfer simulation.

Parameter	Description	Values	Literature reference
$R (R_\odot)$	Stellar radius	5.7	Miotello et al. (2014)
$T (K)$	Blackbody temperature	4880	Miotello et al. (2014)
$L (L_\odot)$	Luminosity	16.5	Miotello et al. (2014)
$M_d (M_\odot)$	Disc mass	0.003	Lommen et al. (2008)
$R_{\text{in}}^{\text{d}} (\text{au})$	Disc inner radius	0.36 ^a	...
$R_{\text{out}}^{\text{d}} (\text{au})$	Disc outer radius	200	Lommen et al. (2008)
$M_{\text{env}} (M_\odot)$	Envelope mass	0.028	Lommen et al. (2008)
$R_{\text{env}}^{\text{in}} (\text{au})$	Envelope inner radius	0.36 ^a	...
$R_{\text{env}}^{\text{out}} (\text{au})$	Envelope outer radius	6000	Motte, Andre & Neri (1998)
$\theta (^\circ)$	Cavity angle	30	Beckford et al. (2008)
$d (\text{pc})$	Distance	120	Boogert et al. (2002)
This article			
χ	Standard UV field	44	see text

Note: ^avalue calculated using $R_{\text{in}} = R_\star (T_\star / T_{\text{in}})^2$ from Dullemond & Monnier (2010).

(VLT–ISAAC). This size is also employed in Lommen et al. (2008) as a fiducial limit.

2.2.2 Dust model

The dust model used in simulations combines bare and covered grains ruled by a Mathis, Rumpl & Nordsieck (MRN) size distribution (Mathis, Rumpl & Nordsieck 1977) ranging between 0.025 and 0.70 μm , constrained using the results of Weingartner & Draine (2001) and Beckford et al. (2008). Bare grains have been used in warm and hot regions (150–1500 K), whereas covered grains were used in cold regions (<150 K), as seen in Lommen et al. (2008). The bare grains are composed of magnesium iron silicate (MgFeSiO_4)⁵ mixed with amorphous carbon,⁶ at proportions of 85 and 15 per cent, respectively. The covered grains, on the other hand, are formed by a dust core (bare grain) and an ice mantle at proportions of 70 per cent for dust and 30 per cent for ice, which is made of CO (5 per cent) and $\text{H}_2\text{O}:\text{CO}_2$ (25 per cent) processed by radiation (Rocha et al. 2017), in order to fit the chemical evolution in the near to mid-IR, as shown in Paper I. The dust opacities are shown in Fig. 7(a) and (b).

2.2.3 External irradiation

The RADMC-3D code simulated an isotropic ISRF by considering an external sphere with the same size of spatial grid as the source of photons. In order to perform the Monte Carlo simulation, photon packages are launched from the sphere inward with the following flux:

$$F_{\text{ISRF}}^{\text{UV}} = \pi W_{\text{dil}} \int_{\Omega} \int_{91\text{nm}}^{205\text{nm}} B_{\lambda}(20\,000 \text{ K}) d\lambda d\Omega, \quad (7)$$

where B_{λ} is a blackbody highly diluted by a factor $W_{\text{dil}} = 8.4 \times 10^{-11}$ by assuming an external radiation field of $44\chi_{\text{ISRF}}$, as described in Section 2.1.2.

⁵http://www.astro.uni-jena.de/Laboratory/OCDB/data/silicate/amorph/olm_g50.lnk

⁶<http://www.astro.uni-jena.de/Laboratory/OCDB/data/carbon/cel800.lnk>

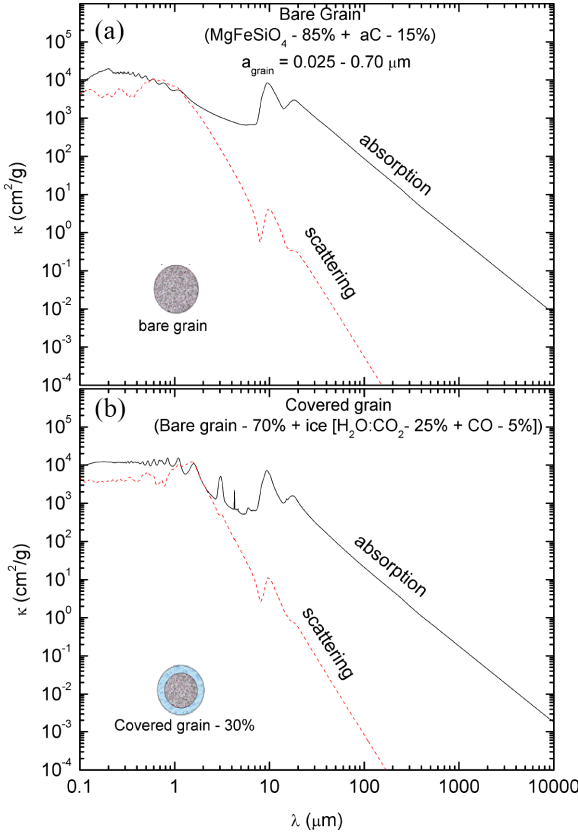


Figure 7. Absorption and scattering opacities of interstellar grains, assuming a MRN size distribution. Panel (a) shows the opacities for bare grains, whereas panel (b) shows the opacities of ice-covered grains.

3 RESULTS

3.1 UV-centimetre SED and near-IR image

The 0.1–100 000 μm spectral energy distribution (SED) of Elias 29 was modelled using RADMC-3D by considering four models taking into account different values of external flux. Models 1–3 adopt $0\chi_{\text{ISRF}}$ ($T_d < 20 \text{ K}$), $100\chi_{\text{ISRF}}$ ($T_d = 35 \text{ K}$) and $44\chi_{\text{ISRF}}$ ($T_d = 30 \text{ K}$), respectively. The best model, called Model 4, consists of Model 3 in addition to greybody emission from the foreground cloud. Such a model reproduces both the near-IR and centimetre emission taken from Lommen et al. (2008) and Miotello et al. (2014).

Fig. 8(a) shows the whole SED of Elias 29, emphasizing the models and observational data from *ISO* and photometric data. Fig. 8(b) shows the SED between 30 and 250 μm , to highlight the contribution of different values of external irradiation between the mid and far-IR. One can observe from Model 1 that a disc+envelope alone cannot reproduce emission for $\lambda > 30 \text{ }\mu\text{m}$, which means that another component contributes to increasing the emission in the mid-IR. Boogert et al. (2002) claims that the ridge temperature is around $15 \pm 5 \text{ K}$, which is low to justify the observed emission in the spectrum. They also report other two components toward Elias 29, with velocities of 2.7 and 3.8 km s^{-1} and temperatures around $15 \pm 5 \text{ K}$ constrained from the intensity ratio of C^{18}O 1-0/3-2. Nevertheless, this value is still low to explain such emission. To overcome this problem, they assume that the second component with velocity 3.8 km s^{-1} should have a temperature between 20 and 40 K . Previous sections in this article, however, have shown that Elias 29 is surrounded by strong UV emission from B-type

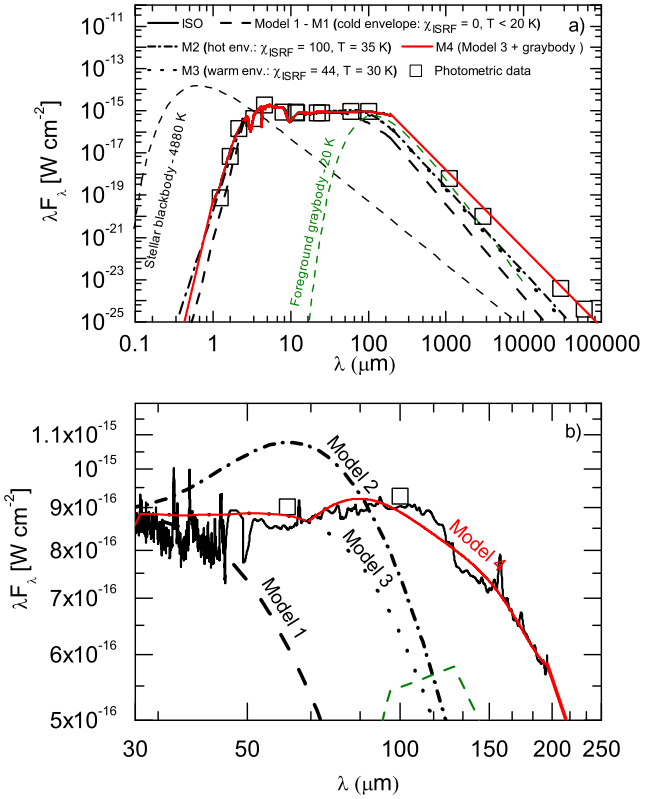


Figure 8. SED of Elias 29 assuming internal and external irradiation. (a) 0.1–100 000 μm SED highlighting Models 1–4 and photometric data taken from literature (Two-Micron All Sky Survey) (2MASS, *Wide-field Infrared Survey Explorer* (WISE), *Spitzer*, *Infrared Astronomical Satellite* (IRAS), Submillimeter Array (SMA) and Australia Telescope Compact Array (ATCA)). (b) Zoom of panel (a) showing details of Models 1–4.

objects and the temperature in its envelope should be around 30 K , constrained from H_2CO rotational lines. Owing to this, there is no reason to consider another foreground component with high temperature, but rather one should assume that Elias 29 contains a warm envelope.

Models 2 and 3 support the idea of an external irradiation not larger than $50\chi_{\text{ISRF}}$ in Elias 29. Once such increasing flux comes from background emission; it is important to calculate the spectrum using the same spectral aperture as *ISO* LWS ($\lambda > 45 \text{ }\mu\text{m}$), i.e. 86 arcsec (Clegg et al. 1996). Nevertheless, the long-wavelength ($\lambda > 100 \text{ }\mu\text{m}$) spectrum is not reproduced in such a scenario and the contribution of a warm foreground cloud should be considered in this case. In this way, Model 4 is the best model to reproduce the Elias 29 spectrum from UV to centimetre regimes.

The structure of Elias 29 was probed by Brandner et al. (2000) using the Infrared Spectrometer and Array Camera (ISAAC) coupled to the Very Large Telescope (VLT) in the H ($1.63-\mu\text{m}$) and K ($2.16-\mu\text{m}$) bands in polarimetric mode. The authors report a bipolar nebula structure in the K band with a field of view (FOV) of 1 arcmin. Huélamo et al. (2005), in addition, probed the inner structure of Elias 29 with a FOV of 3 arcsec using NaCo (short for Nasmyth Adaptive Optics System - NAOS and Near-Infrared Imager and Spectrograph - CONICA) polarimetric differential imaging. A dark lane is detected in the north-east–south-west direction, indicating the presence of a protostellar disc with radius larger than 180 au.

In Paper I, modelling of Elias 29 in the K band considering only an internal source of irradiation is presented. In this article, how-

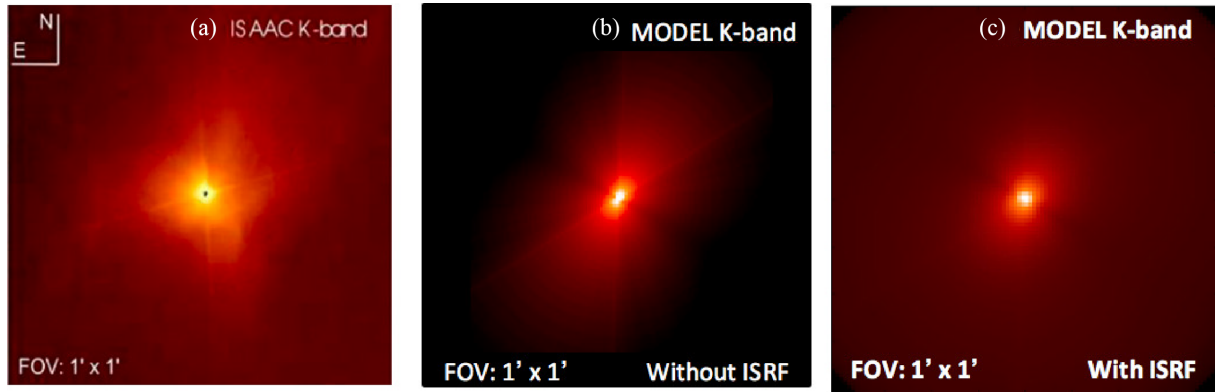


Figure 9. Comparison between observations and model of Elias 29 as seen in the K band ($2.16 \mu\text{m}$). Panel (a) shows Elias 29 as observed with ISAAC/VLT in polarimetric mode (adapted from Huélamo et al. 2005). Panels (b) and (c) show Elias 29 simulated with RADMC-3D assuming scenarios without and with external irradiation, respectively. No polarization is calculated in the models.

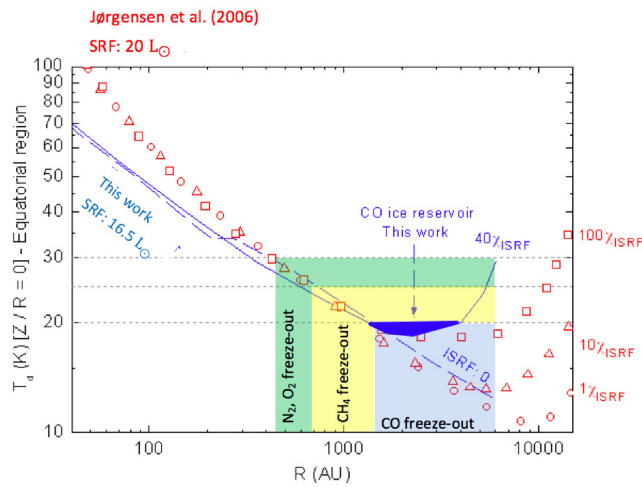


Figure 10. 1D dust temperature profiles as a function of radius. Dashed and solid blue lines are relative to Elias 29 Models 1 and 4, respectively. Red symbols concern models described in Jørgensen et al. (2006) for χ/χ_{ISRF} of 1, 10 and 100. The freeze-out regions of volatile species are also indicated by the coloured regions. A dark blue region highlights the CO ice reservoir in Elias 29.

ever, external irradiation is included in the simulation, according to Model 4. This methodology was employed in Gramajo et al. (2010) by combining SED + an image approached by eye to obtain more reliable results. The real image of Elias 29 is shown in Fig. 9(a) (Huélamo et al. 2005) and the synthetic image in Fig. 9(c). Fig. 9(b) shows modelling without external irradiation, as considered in Model 1. The brightness profile that highlights bipolar nebulosity in the real image (Fig. 9a), compared with Models 1 and 4, comes from scattered polarized light, once such an image was observed in polarimetric mode.

3.2 Temperature distribution

The routine *mctherm* in RADMC-3D was used to calculate the dust temperature of Elias 29. Fig. 10 compares the 1D temperature profiles for Models 1 and 4 with the work of Jørgensen et al. (2006), which illustrates the competition between internal and external heating for an envelope. The numerical density at the outer radius is for a range between 50 and 15 000 au.

The models in Jørgensen et al. assume an internal source with $20 L_\odot$ and different χ_{ISRF} values of 1, 10 and 100. One can observe that even typical interstellar radiation ($1\chi_{\text{ISRF}}$) might heat the outer envelope by a few degrees. However, only after $10\chi_{\text{ISRF}}$ is the temperature increased above 20 K, which might present important consequences for chemistry once CO ice desorbs around 18–20 K (Collings et al. 2004). From the Elias 29 models, it is possible to observe that an external irradiation of $44\chi_{\text{ISRF}}$ increases the outer envelope up to 30 K and, between 1500 and 4000 au, forms a CO ice reservoir. Such a temperature profile, including external irradiation, was also described in Launhardt et al. (2013) for starless and protostellar cores. They show that the variation of observed mean outer dust temperature ($\Delta T_d^{\text{outer}}$) for a dataset of 12 globules is around 5 K, by considering a χ of 5 and $A_V = 4$ mag. Such a result is also similar to the models of Jørgensen et al. and supports the idea that strong external irradiation is necessary to drive significant chemical changes in the envelope.

Fig. 11 shows the 2D temperature profile of Elias 29, emphasizing the disc and envelope. The scenario without external irradiation, as shown in panels (a1) and (a2), was already described in detail in Paper I, in which only the internal protostar is a source of heating. In this article, however, we present a new discussion considering an external source of UV photons, as seen in panels (b1) and (b2). By comparing both panels, one can observe that external irradiation might redefine the snowline position of volatile species such as N_2 and O_2 ice, CH_4 ice and CO ice that desorbs at 30, 25 and 20 K, respectively, according to laboratory experiments detailed in Collings et al. (2004). In the presence of an external UV field, the snowlines change from a layered structure to a toroidal-shaped distribution. Despite the species being volatile, they might survive in low abundance up to a temperature of 150 K, if they are trapped in a H_2O ice matrix that represents the most realistic scenario.

CO ice has an important role for complex chemistry in the solid phase and many laboratory experiments have shown that repeated hydrogenation of the adsorbed CO on dust grains leads to the formation of H_2CO and CH_3OH (Watanabe & Kouchi 2002; Watanabe, Shiraki & Kouchi 2003; Fuchs et al. 2009). Nevertheless, the methanol ice formation by this pathway is highly dependent on the temperature (Watanabe et al. 2003). The authors claim that the maximum yield of CH_3OH ice formation is reached for temperatures between 10 and 15 K, whereas at 20 K the abundance of this ice is significantly smaller. Further, Monte Carlo simulations from Cuppen et al. (2009) have demonstrated that, in regions with densities n

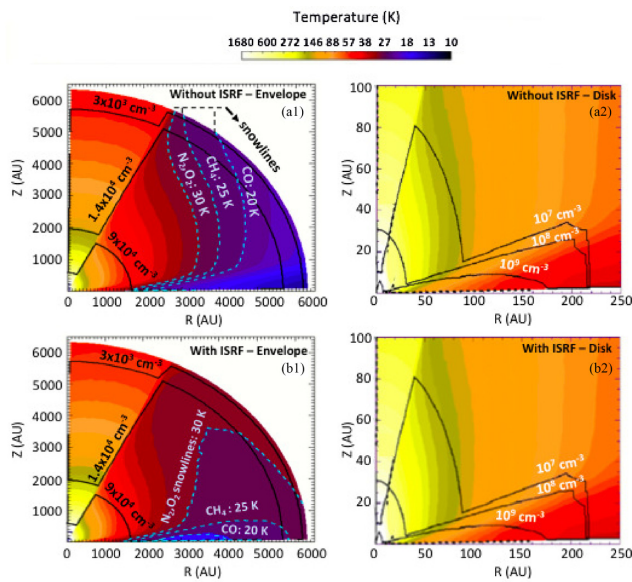


Figure 11. Temperature map of Elias 29 including and excluding the ISRF (Models 4 and 1, respectively). Solid lines represent the H_2 densities and dashed lines the snowlines for CO (20 K), CH_4 (25 K) and N_2, O_2 (30 K). A cold toroidal-shaped region in the envelope can be easily observed in panel (b1). Nothing changes in the disc region.

$\geq 10^5 \text{ cm}^{-3}$ and a large H/CO ratio at low temperature, both H_2CO and CH_3OH ices are formed on a short time-scale, which suggests that methanol ice can be present from the first stages of the star-formation process onwards. Another mechanism to form CH_3OH ice was presented in Bergner et al. (2017), in which the authors employed the insertion of O atoms into CH_4 ice for temperatures below 25 K.

The gas abundance of Elias 29 was reported in Boogert et al. (2000), showing that CO is the most abundant gas, followed by H_2O and CO_2 , with gas/solid ratios of around 53, 0.23 and 0.011, respectively. Rotational diagrams for CO gas indicate two populations as detailed in Boogert et al. (2002): (i) hot CO at 1100 K and $N_{\text{hot}}(\text{CO}) = 2 \times 10^{18} \text{ cm}^{-2}$, (ii) cold CO at 90 K and $N_{\text{cold}}(\text{CO}) = (16 \pm 10) \times 10^{18} \text{ cm}^{-2}$, which indicates that CO gas is present in Elias 29 itself. H_2O and OH are also placed in Elias 29, once the rotational diagrams trace temperatures of 379 and 230 K, respectively.

H_2CO and CH_3OH were also observed in the gas phase toward Elias 29, as indicated in Boogert et al. (2002). The V_{LSR} of both molecules indicates that p- H_2CO transitions above 145 GHz belong to the outer envelope of Elias 29, whereas the transition 2–1 triplet of CH_3OH at 96 GHz belongs to foreground clouds. Once no other large molecule is observed in the Elias 29 direction, this could be indicative that complex species are confined by the snowlines presented in Fig. 11 and are not observed due to an inclination of 60° .

The right-hand panels of Fig. 11 emphasize the disc region in both models. One can observe that the dust temperature is still the same and external irradiation does not have an influence for $R < 250$ au. Even FUV photons coming through the low-density cavity are extinguished at radius $R > 4500$ au in this model, due to small dust grains. The snowlines of volatile species such as N_2, O_2 and CH_4 are not shown, once the outer disc presents a temperature around 70 K. Even in this situation, volatile species might be present if trapped in non-volatile ice, for example H_2O or CO_2 .

4 CONCLUSIONS

In this article, the interplay between external UV and the stellar radiation field, with the survival of astrophysical ices, was addressed. Specifically, we introduced a discussion about the formation of a toroidal-shaped region of volatile compounds limited by their snowlines at the outer envelope of Elias 29. The conclusions are summarized below.

(i) The outer envelope of Elias 29 is more warm ($T \sim 30$ K) than expected for protostars illuminated only by a central source of photons. Such a temperature is justified by the presence of many YSOs around Elias 29 distant only by 3 arcmin, as well as by two bright B-type stars (S1 and HD 147889). Comparatively, HD 147889 contributes 93 per cent of the FUV emission in the ρ Oph cloud and produces external irradiation of around $44\chi_{\text{ISRF}}$ in Elias 29. In such a scenario, the background emission observed in the K band is reproduced approximately.

(ii) In the Elias 29 environment, the FUV external irradiation might penetrate the envelope and redefine the snowline position of volatile molecules such as N_2, O_2, CH_4 and CO to a toroidal-shaped form. In that case, the maximum abundance of CO ice is confined to a small region of the envelope and, consequently, the abundance of complex molecules as a result of hydrogenation and oxygenation mechanisms is expected to be severely reduced. To address the impact of external irradiation on the survival of complex organic molecules, this model will be used as a template for the physico-chemical PRODIMO code (Woitke, Kamp & Thi 2009; Kamp et al. 2010; Thi, Woitke & Kamp 2011; Woitke et al. 2016; Kamp et al. 2017) in a forthcoming article.

(iii) Although the scheme of a toroidal region of volatile compounds, such as found in Elias 29, is exciting, this might not be a global scenario once the closest YSOs do not contribute much to increasing the ISRF (roughly 2 per cent). Nevertheless, other regions, such as CrA and ρ Oph A, are also dominated by external irradiation and a comprehensive modelling of the chemistry in these objects will improve our knowledge of the chemical heritage in environments that are externally irradiated.

ACKNOWLEDGEMENTS

The authors thank FAPESP (PD 2015/10492-3) for the financial support of this work and also FVE/UNIVAP and CAPES. We acknowledge the positive comments from an anonymous referee, which improved this manuscript greatly, as well as private communications with Dr Joel D. Green about Herschel observations toward the ρ Oph cloud. Finally, we thank Dr Peter Woitke for all his comments regarding this article.

REFERENCES

- Beckford A. F., Lucas P. W., Chrysostomou A. C., Gledhill T. M., 2008, *MNRAS*, 384, 907
- Bergner J. B., Öberg K. I., Garrod R. T., Graninger D. M., 2017, *ApJ*, 841, 120
- Bontemps S. et al., 2001, *A&A*, 372, 173
- Boogert A. C. A., Tielens A. G. G. M., Ceccarelli C., Boorman A. M. S., van Dishoeck E. F., Keane J. V., Whittet D. C. B., de Graauw T., 2000, *A&A*, 360, 683
- Boogert A. C. A., Hogerheijde M. R., Ceccarelli C., Tielens A. G. G. M., van Dishoeck E. F., Blake G. A., Latter W. B., Motte F., 2002, *ApJ*, 570, 708
- Brandner W. et al., 2000, *A&A*, 364, L13

- Ceccarelli C., Boogert A. C. A., Tielens A. G. G. M., Caux E., Hogerheijde M. R., Parise B., 2002, *A&A*, 395, 863
- Chiang E. I., Goldreich P., 1997, *ApJ*, 490, 368
- Clegg P. E. et al., 1996, *A&A*, 315, L38
- Collings M. P., Anderson M. A., Chen R., Dever J. W., Viti S., Williams D. A., McCoustra M. R. S., 2004, *MNRAS*, 354, 1133
- Crapsi A., van Dishoeck E. F., Hogerheijde M. R., Pontoppidan K. M., Dullemond C. P., 2008, *A&A*, 486, 245
- Cuppen H. M., van Dishoeck E. F., Herbst E., Tielens A. G. G. M., 2009, *A&A*, 508, 275
- de Geus E. J., de Zeeuw P. T., Lub J., 1989, *A&A*, 216, 44
- Draine B. T., 2003, *ARA&A*, 41, 241
- Draine B. T., Bertoldi F., 1996, *ApJ*, 468, 269
- Dullemond C. P., Monnier J. D., 2010, *ARA&A*, 48, 205
- Fitzpatrick E. L., 1999, *PASP*, 111, 63
- Fuchs G. W., Cuppen H. M., Ioppolo S., Romanzin C., Bisschop S. E., Andersson S., van Dishoeck E. F., Linnartz H., 2009, *A&A*, 505, 629
- Goldsmith P. F., Langer W. D., 1999, *ApJ*, 517, 209
- Gramajo L. V., Whitney B. A., Gómez M., Robitaille T. P., 2010, *AJ*, 139, 2504
- Green J. D. et al., 2013, *ApJ*, 770, 123
- Green J. D. et al., 2016, *AJ*, 151, 75
- Huélamo N., Brandner W., Wolf S., Khanzadyan T., 2005, Proc. Conf. LPI Contribution No. 1286, Protostars and Planets V. Hilton Waikoloa Village, Hawai'i, p. 8209
- Je H., Lee J.-E., Lee S., Green J. D., Evans N. J., II, 2015, *ApJS*, 217, 6
- Jørgensen J. K., Johnstone D., van Dishoeck E. F., Doty S. D., 2006, *A&A*, 449, 609
- Jørgensen J. K., Johnstone D., Kirk H., Myers P. C., Allen L. E., Shirley Y. L., 2008, *ApJ*, 683, 822
- Kamp I., Tilling I., Woitke P., Thi W.-F., Hogerheijde M., 2010, *A&A*, 510, A18
- Kamp I., Thi W.-F., Woitke P., Rab C., Bouma S., Ménard F., 2017, *A&A*, 607, A41
- Khanzadyan T., Gredel R., Smith M. D., Stanke T., 2004, *A&A*, 426, 171
- Klessen R. S., Burkert A., Bate M. R., 1998, *ApJ*, 501, L205
- Larson R. B., 1978, *MNRAS*, 184, 69
- Larsson B., Liseau R., 2017, *A&A*, 608, A133
- Launhardt R. et al., 2013, *A&A*, 551, A98
- Lee S., Lee J.-E., Bergin E. A., 2015, *ApJS*, 217, 30
- Lindberg J. E., Jørgensen J. K., 2012, *A&A*, 548, A24
- Lindberg J. E. et al., 2014, *A&A*, 566, A74
- Lindberg J. E., Charnley S. B., Jørgensen J. K., Cordiner M. A., Bjerkeli P., 2017, *ApJ*, 835, 3
- Liseau R. et al., 1999, *A&A*, 344, 342
- Liseau R. et al., 2015, *A&A*, 578, A131
- Lommen D., Jørgensen J. K., van Dishoeck E. F., Crapsi A., 2008, *A&A*, 481, 141
- Mathis J. S., Rumpl W., Nordsieck K. H., 1977, *ApJ*, 217, 425
- Miotello A., Testi L., Lodato G., Ricci L., Rosotti G., Brooks K., Maury A., Natta A., 2014, *A&A*, 567, A32
- Motte F., Andre P., Neri R., 1998, *A&A*, 336, 150
- Müller H. S. P., Thorwirth S., Roth D. A., Winnewisser G., 2001, *A&A*, 370, L49
- Ortiz-León G. N. et al., 2017, *ApJ*, 834, 141
- Pontoppidan K. M., Dullemond C. P., van Dishoeck E. F., Blake G. A., Boogert A. C. A., Evans N. J., II, Kessler-Silacci J. E., Lahuis F., 2005, *ApJ*, 622, 463
- Ressler M. E., Barsony M., 2001, *AJ*, 121, 1098
- Ridge N. A. et al., 2006, *AJ*, 131, 2921
- Riviere-Marichalar P., Merín B., Kamp I., Eiroa C., Montesinos B., 2016, *A&A*, 594, A59
- Rocha W. R. M., Pilling S., 2015, *ApJ*, 803, 18 (Paper I)
- Rocha W. R. M., Pilling S., de Barros A. L. F., Andrade D. P. P., Rothard H., Boduch P., 2017, *MNRAS*, 464, 754
- Röllig M. et al., 2007, *A&A*, 467, 187
- Thi W.-F., Woitke P., Kamp I., 2011, *MNRAS*, 412, 711
- van Dishoeck E. F., Jonkheid B., van Hemert M. C., 2006, *Faraday Discussions*, 133, 231
- Watanabe N., Kouchi A., 2002, *ApJ*, 571, L173
- Watanabe N., Shiraki T., Kouchi A., 2003, *ApJ*, 588, L121
- Weingartner J. C., Draine B. T., 2001, *ApJ*, 548, 296
- Woitke P., Kamp I., Thi W.-F., 2009, *A&A*, 501, 383
- Woitke P. et al., 2016, *A&A*, 586, A103
- Zhang H. et al., 2017, *MNRAS*, 465, 2983

This paper has been typeset from a \TeX / \LaTeX file prepared by the author.